

## Design of Active and Stable Oxygen Reduction Reaction Catalysts by Embedding $\text{Co}_x\text{O}_y$ Nanoparticles into Nitrogen-Doped Carbon

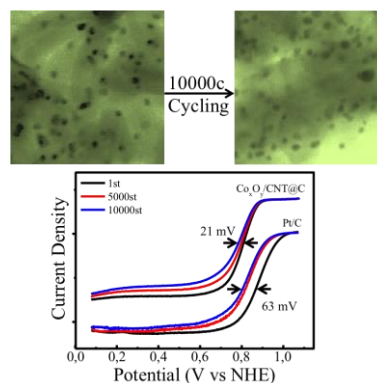
Fan Yang<sup>1</sup>, Mikel Abadia<sup>2</sup>, Chaoqiu Chen<sup>1</sup>, Weike Wang<sup>1</sup>, Le Li<sup>1</sup>, Lianbing Zhang<sup>1</sup>, \* Celia Rogero<sup>2, 3</sup>, Andrey Chuvilin<sup>1, 4</sup>, and Mato Knez<sup>1, 4, \*</sup>

<sup>1</sup>CIC nanoGUNE Consolider, Tolosa Hiribidea 76, 20018 Donostia-San Sebastian, Spain

<sup>2</sup>Centro de Física de Materiales, Paseo Manuel de Lardizabal, 5, 20018 Donostia-San Sebastian, Spain

<sup>3</sup>Donostia International Physics Center (DIPC), Paseo Manuel de Lardizabal, 4, 20018 Donostia-San Sebastian, Spain

<sup>4</sup>IKERBASQUE, Basque Foundation for Science, Maria Diaz de Haro 3, 48013 Bilbao, Spain



$\text{Co}_x\text{O}_y$  nanoparticles are uniformly deposited on carbon nanotubes (CNTs) by atomic layer deposition, and covered by a N-doped carbon layer. The material exhibits excellent oxygen reduction reaction reactivity. More importantly, the N-doped carbon shell prevents nanoparticles agglomeration and leaching from the CNTs, leading to exceptional stability/durability over long-term operation.

Provide the authors' website if possible.

Author 1, website 1

Author 2, website 2



# Design of Active and Stable Oxygen Reduction Reaction Catalysts by Embedding $\text{Co}_x\text{O}_y$ Nanoparticles into Nitrogen-Doped Carbon

Fan Yang<sup>1</sup>, Mikel Abadia<sup>2</sup>, Chaoqiu Chen<sup>1</sup>, Weike Wang<sup>1</sup>, Le Li<sup>1</sup>, Lianbing Zhang<sup>1</sup> (✉), Celia Rogero<sup>2, 3</sup>, Andrey Chuvilin<sup>1, 4</sup>, and Mato Knez<sup>1, 4</sup> (✉)

<sup>1</sup>CIC nanoGUNE Consolider, Tolosa Hiribidea 76, 20018 Donostia-San Sebastian, Spain

<sup>2</sup>Centro de Física de Materiales, Paseo Manuel de Lardizabal, 5, 20018 Donostia-San Sebastian, Spain

<sup>3</sup>Donostia International Physics Center (DIPC), Paseo Manuel de Lardizabal, 4, 20018 Donostia-San Sebastian, Spain

<sup>4</sup>IKERBASQUE, Basque Foundation for Science, Maria Diaz de Haro 3, 48013 Bilbao, Spain

**Received:** day month year

**Revised:** day month year

**Accepted:** day month year  
(automatically inserted by  
the publisher)

© Tsinghua University Press  
and Springer-Verlag Berlin  
Heidelberg 2016

## KEYWORDS

Atomic layer deposition,  
Cobalt Oxide,  
Polydopamine, Oxygen  
Reduction Reaction

## ABSTRACT

The oxygen reduction reaction (ORR) is essential for both life science and energy related research. In applications, platinum based catalysts are a good choice for the ideal reactivity, but in practice those are often subject to high cost and poor stability. Some cost-efficient transition metal oxides were found to exhibit excellent ORR reactivity, but the stability and durability of such alternative catalyst materials pose serious challenges. Here, we present a facile method to fabricate uniform  $\text{Co}_x\text{O}_y$  nanoparticles and embed them into N-doped carbon, which results in an extraordinary stability/durability of the composite while maintaining its high reactivity. The half wave potential shows a negative shift of only 21 mV after 10000 cycles, which is one third of that observed from the Pt/C system (63 mV). Furthermore, after 100000 s testing at a constant potential the current decreases by only 17%, significantly less than in the case of Pt/C (35%). The exceptional stability/durability is resulting from the architecture of the system: a thin carbon shell prevents agglomeration of the  $\text{Co}_x\text{O}_y$  nanoparticles and their detaching from the substrate.

## 1 Introduction

Among the largest obstacles for a massive use of a variety of fuel cells or metal-air batteries is the sluggish kinetics of the oxygen reduction reaction (ORR) at the cathode [1–3]. The ORR catalyst

determines with great share the overall performance of the device or system, which makes it a crucially important component. Seemingly, a set of good catalysts has been identified with platinum or its alloys exhibiting exceptional catalytic performance and efficiency [4–6]. However, use of platinum in large quantities for mass production is economically

Address correspondence to Lianbing Zhang, lzhang@nanogune.eu; Mato Knez, mknez@nanogune.eu

not feasible. Moreover, Pt-based catalysts often suffer from electrochemical and temporal instability, which is primarily a result of the highly reactive Pt-based nanostructures. The stability of a catalyst in long-term operation is considered to be one of the most important hurdles to be overcome for implantation into real devices and commercialization. Thus, finding cheap, efficient and stable alternatives to Pt for the ORR is highly desired.

The recent years have witnessed a tremendous progress in identifying and characterizing such cost-effective and efficient catalysts for the ORR, like nitrogen (N) or transition metal (M) doped carbon or M-N co-doped carbon [7–10]. Besides carbon-based materials, transition metal oxides came into focus as good alternatives for the noble metal based ORR catalysts. In various attempts,  $\text{Fe}_3\text{O}_4$  [11,12],  $\text{Co}_3\text{O}_4$  [13,14],  $\text{CoO}$  [15–18] and some further oxides [19–25] were shown to be excellent candidates. Those often have comparable or sometimes even slightly better reactivity than Pt, which gives rise to optimism for finding a suitable system to replace Pt, at least from the perspective of activity. However, the stability/durability for long-term operation still remains being a great challenge [26].

The proposed metal oxide-based catalysts for ORR consist of a variety of nanostructures. The collapse of nanostructures, like leaching or agglomeration of active materials seriously contribute to the instability of the catalyst [26]. Maintaining this nano-architecture during operation is expected to ensure long-term stability and preserve high activity, but this is a great challenge. In the following, we describe our approach towards stabilizing the ORR catalyst. The system is based on  $\text{Co}_x\text{O}_y$  nanoparticles that are grown on carbon nanotubes (CNTs). For stabilization, the system was covered with a thin N-doped carbon shell by coating the CNT-nanoparticle composite with polydopamine (PDA) and subsequent pyrolysis. The final construct of nanoparticles, CNTs and doped carbon will in the following be referred to as  $\text{Co}_x\text{O}_y/\text{CNT}@C$ . The stability and durability of the  $\text{Co}_x\text{O}_y/\text{CNT}@C$ , if compared to the commercial Pt/C, is truly exceptional. After a standard cycling test, the half wave potential of  $\text{Co}_x\text{O}_y/\text{CNT}@C$  showed a negative shift of only 21 mV after 10000 cycles, which is one third of that observed with the commercial Pt/C (63

mV). Furthermore, after 100000 s operation at a constant potential the current decreased by only 17%, which is only half of the decrease observed from Pt/C (35%). This exceptional stability and durability of  $\text{Co}_x\text{O}_y/\text{CNT}@C$  is a result of the special architecture, in which the N-doped carbon shell prevents the embedded  $\text{Co}_x\text{O}_y$  nanoparticles from agglomeration and detaching off of the CNTs. This synthetic strategy and the resulting nano-architecture are not specific for this problem but may also be applied more universally, showing promise for a plethora of further energy-related or catalytic applications.

## 2 Experimental

### 2.1 Materials synthesis

Atomic layer deposition (ALD) was used to deposit  $\text{Co}_3\text{O}_4$  onto commercial multi-walled carbon nanotubes (MNCNTs) in a commercial ALD coater (Savannah 100, Cambridge Nanotech Inc.). Bis(cyclopentadienyl)-cobalt(II) ( $\text{Co}(\text{Cp})_2$ ) and  $\text{O}_3$  were used as cobalt and oxygen source. The reactor was kept at 200 °C, and the  $\text{Co}(\text{Cp})_2$  source was maintained at 65 °C. High purity  $\text{N}_2$  (99.99%) was used as both carrier and purging gas. All gas lines were kept at 120 °C to prevent cold spots and precursor condensation. For each ALD cycle, the pulse time, exposure time and purging time of  $\text{Co}(\text{Cp})_2$  and  $\text{O}_3$  precursors were 1 s/60 s/90 s and 0.8 s/60 s/90 s, respectively.

CNT or  $\text{Co}_3\text{O}_4/\text{CNT}$  were then dispersed in water (6 mg/mL), then mixed with 60 mM Tris buffer (PH 8.8) and 6 mg/mL dopamine solution by 1:1:1. The mixed solution was stirred for 24 hours at room temperature. Afterwards, the samples were washed by centrifugation with water for at least three times, then dried and collected.

The collected  $\text{Co}_3\text{O}_4/\text{CNT}$ ,  $\text{CNT}@PDA$  and  $\text{Co}_3\text{O}_4/\text{CNT}@PDA$  samples were annealed in an oven at elevated temperatures (400 to 800 °C) under  $\text{N}_2$  flow in vacuum (around 3 mbar) for 2 hours individually. The  $\text{Co}_3\text{O}_4/\text{CNT}$ ,  $\text{CNT}@PDA$  or  $\text{Co}_3\text{O}_4/\text{CNT}@PDA$  were also annealed in-situ in an XPS chamber while measuring.

## 2.2 Physical characterization.

Electron microscopy samples were prepared by drop-drying ethanol suspensions of the samples onto copper grids. The morphologies and microstructures of the synthesized samples were characterized with scanning transmission electron microscopy (FEI, Helios 450S), and transmission electron microscopy (FEI, Titan G2 60-300) was carried out to characterize the structure of the nanoparticles and to perform element analysis at higher magnifications. XRD examinations were performed with a powder diffractometer (X'pert, PANalytical). XPS experiments were performed using a Phoibos photoelectron spectrometer equipped with an Al K $\alpha$  X-ray source as the incident photon radiation. Samples were drop-dried onto silicon or gold substrates, using the Si 2p or the Au 4f signals for binding energy calibration. In-situ heating experiments were performed inside the UHV chamber, with a base pressure of 10<sup>-9</sup> mbar. XPS spectra of Co 2p, O 1s, N 1s and C 1s core levels were measured for Co<sub>3</sub>O<sub>4</sub>/CNT, CNT@PDA and Co<sub>3</sub>O<sub>4</sub>/CNT@PDA as received (RT) and after annealing processes at 400 °C (below the ex-situ annealing process) and at 600 °C (ex-situ annealing process).

## 2.3 Electrochemical characterization.

For the catalyst preparation, 2 mg of a sample was dispersed in 750  $\mu$ l of water, 200  $\mu$ l of ethanol and 50  $\mu$ l of Nafion solution (5 wt.%), and then ultrasonicated for 15 min to form homogeneous ink. For the electrochemical measurements 20  $\mu$ l of the catalyst ink was loaded onto a glassy carbon electrode of 5 mm in diameter (loading 0.20 mg/cm<sup>2</sup>). Commercial Pt/C catalyst samples were prepared in the same way. The catalytic performances of the catalysts were analyzed with a standard three-electrode system with a Pt sheet as counter electrode and Ag/AgCl (3 M KCl) as reference electrode in 0.1 M KOH solution. The electrolyte was saturated with O<sub>2</sub> (or N<sub>2</sub>) by bubbling O<sub>2</sub> (or N<sub>2</sub>) prior to the start of each

experiment. Cyclic voltammetry (CV) tests were performed in both O<sub>2</sub> and N<sub>2</sub> saturated 0.1 M KOH electrolytes at a scanning rate of 50 mV/s. Before recording the data, the electrodes were cycled at least 5 times until a stable curve was obtained. Linear sweep voltammetry (LSV) was also carried out in O<sub>2</sub> saturated 0.1 M KOH at a scanning rate of 10 mV/s with a rotating electrode speed range from 400 to 2500 rpm. The Koutecky–Levich plots (J<sup>-1</sup> vs.  $\omega^{-1/2}$ ) were analyzed at various electrode potentials. The slopes of their linear fit lines were used to calculate the number of electrons transferred (n) based on the Koutecky-Levich equation below:

$$\frac{1}{J} = \frac{1}{J_L} + \frac{1}{J_K} = \frac{1}{B\omega^{1/2}} + \frac{1}{J_K}$$

$$B = 0.62nFC_0(D_0)^{2/3}\nu^{-1/6} \quad J_K = nFkC_0$$

where J is the measured current density, J<sub>L</sub> is the diffusion-limiting current density, J<sub>K</sub> is the kinetic-diffusion-limiting current density,  $\omega$  is the angular velocity, n is the electron number transferred, F is the Faraday constant, C<sub>0</sub> is the bulk concentration of O<sub>2</sub>,  $\nu$  is the kinematic viscosity of the electrolyte, and k is the electron-transfer rate constant. For the Tafel plot, the kinetic current density was calculated according to the equation:

$$J_K = \frac{J * J_L}{J_L - J}$$

The cycling stabilities were characterized using CVs with a small potential window at high scanning rates of 500 mV/s for 10,000 cycles. After every 1,000 cycles LSVs were recorded (scanning rate 10 mV/s, rotating speed 1600 rpm). The durability tests were carried out by chronoamperometry at a bias potential of 0.65 V (vs. RHE) for 100,000 s in the constantly O<sub>2</sub>-saturated electrolyte with a rotating speed of 1600 rpm. The electrochemical tests were performed in O<sub>2</sub>-saturated electrolyte with a rotating speed of 1600 rpm at the potential of -0.15 V vs. Ag/AgCl. All electrochemical tests were carried out using an Autolab electrochemical working station (PGSTAT 302N).

### 3 Results and discussion

Atomic layer deposition (ALD) was applied to deposit cobalt oxide onto commercial carbon nanotubes (CNTs, Figure 1a), as it offers the possibility to grow uniformly distributed oxide nanoparticles on complex surfaces or structures with extreme control [27,28]. Cobaltocene ( $\text{CoCp}_2$ ) and  $\text{O}_3$  were used as metal and oxygen sources. In our earlier work [29,30], we demonstrated that  $\text{O}_3$  preferentially oxidizes the carbonaceous debris on the outer wall of CNTs, creating functional groups or defects. These functional groups or defects act as anchoring sites for the chemisorption of  $\text{CoCp}_2$  during the initiation of ALD growth. Subsequently supplied  $\text{O}_3$  will react with the immobilized Co precursor to produce  $\text{Co}_3\text{O}_4$ . Due to the discrete anchoring sites on the otherwise inert surfaces of the CNTs, an island growth rather than a compact film growth is favored [31]. After the initial few cycles,  $\text{Co}_3\text{O}_4$  seeds are formed on the CNTs, which in the continuation of the process act as preferential sites for further  $\text{Co}_3\text{O}_4$  deposition, giving rise to a particle growth throughout the deposition process. Consequently, uniformly distributed  $\text{Co}_3\text{O}_4$

nanoparticles are formed on CNTs (Figure 1b). By altering the number of ALD cycles, the size of nanoparticles can be further optimized (Figure S1).

After the  $\text{Co}_3\text{O}_4$  deposition,  $\text{Co}_3\text{O}_4/\text{CNT}$ s were further coated with a thin layer of polydopamine (PDA) (Figure 1c) by mixing with a dopamine solution and gentle stirring at room temperature, as dopamine tends to oxidative self-polymerize in appropriate pH environment [32–34]. An inspection of a PDA-coated sample with STEM (Figure S2) revealed that the PDA layer uniformly covered the surface of the CNTs, including the  $\text{Co}_3\text{O}_4$  nanoparticles. In the next step, the  $\text{Co}_3\text{O}_4/\text{CNT}@PDA$  samples were annealed at elevated temperatures in a  $\text{N}_2$  atmosphere. The annealing resulted in the PDA polymer decomposing to an embedding carbon shell and a slight growth of the nanoparticle due to some limited Ostwald ripening (Figure 1d). High resolution TEM was applied to characterize the annealed sample ( $\text{Co}_x\text{O}_y/\text{CNT}@C$ ). Figure 1e shows that the oxide nanoparticles were still embedded in the carbon shell after annealing, but the lattice fringes indicate that the oxidation state of the nanoparticles has changed during the process.

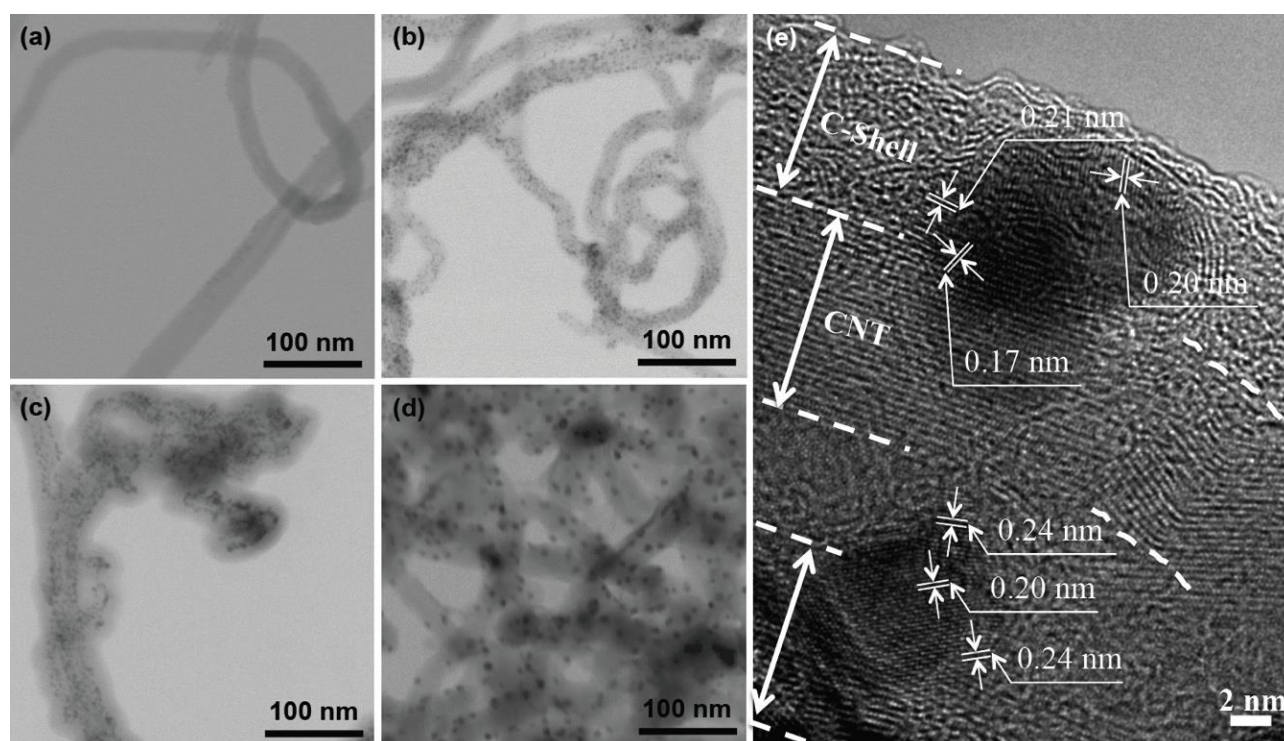


**Figure 1.** STEM images of a) pristine CNTs and b)  $\text{Co}_3\text{O}_4$  nanoparticles grown on CNTs by ALD ( $\text{Co}_3\text{O}_4/\text{CNT}$ ); c) PDA-coated  $\text{Co}_3\text{O}_4/\text{CNT}$  ( $\text{Co}_3\text{O}_4/\text{CNT}@PDA$ ), and d)  $\text{Co}_3\text{O}_4/\text{CNT}@PDA$  after annealing at  $600\text{ }^\circ\text{C}$  in  $\text{N}_2$  atmosphere ( $\text{Co}_x\text{O}_y/\text{CNT}@C$ ), and e) HRTEM image of  $\text{Co}_x\text{O}_y/\text{CNT}@C$ .

X-ray diffraction patterns were collected to trace the evolution of the oxide nanoparticles upon annealing. In Figure 2a, the peak at  $26.2^\circ$  corresponds to the (002) plane of CNTs, while clear peaks at  $31.2^\circ$ ,  $36.7^\circ$ ,  $44.7^\circ$ ,  $59.2^\circ$  and  $65.2^\circ$  for  $\text{Co}_3\text{O}_4/\text{CNT}$  occur, corresponding to (022), (113), (004), (115) and (044) planes of  $\text{Co}_3\text{O}_4$ , respectively. After annealing, new peaks at  $44.2^\circ$  and  $51.4^\circ$  appear, associated to (111) and (002) planes of Co metal, while all peaks characteristic for  $\text{Co}_3\text{O}_4$  decrease or even disappear. Further annealing conditions (at  $800^\circ\text{C}$ ), reduce the oxide to Co metal with all peaks in the XRD spectrum corresponding to the cubic structure of Co (Figure S3). This is consistent with previous observations:  $\text{Co}_3\text{O}_4$  releases O during heating under  $\text{N}_2$  flow, converting into CoO or even metallic Co [35–37]. Interestingly, element mapping of Co and O with Energy-Dispersive X-Ray spectroscopy (Figure S4) shows that  $\text{Co}_3\text{O}_4$  nanoparticles transformed into core-shell particles with a metallic core and an oxide shell. From HRTEM, in the outer shell the measured interplanar spacings of 0.24 nm and 0.20 nm may correspond to (113) and (004) planes of  $\text{Co}_3\text{O}_4$ ; alternatively, the 0.24 nm and 0.21 nm may correspond to (111) and (002) planes of cubic CoO; while the spacings of 0.20 nm and 0.17 nm in the inner core correspond to (111) and (002) planes of metallic Co. Note that according to the XRD spectrum of  $\text{Co}_x\text{O}_y/\text{CNT}@C$ , presence of some CoO phases, for example the (111) plane, may be possible, but with  $36.4^\circ$  it is too close to the (113) plane of  $\text{Co}_3\text{O}_4$  at  $36.7^\circ$  to be clearly distinguished.

X-ray photoelectron spectroscopy (XPS) was used to analyze the elemental information of the synthesized materials. After the ALD process clear Co 2p core level peaks at around Co  $2p_{3/2}$  and Co  $2p_{1/2}$  appeared accompanied with two satellites, corresponding to the energy position of  $\text{Co}_3\text{O}_4$  (Figure 2b) [38,39]. For  $\text{Co}_3\text{O}_4/\text{CNT}@PDA$ , the intensity of the Co 2p peaks was nearly zero because the mean free path of the excited photoelectrons is shorter than the thickness of PDA layer. This suggests that all the nanoparticles and CNT were completely embedded into the PDA. After annealing, both Co  $2p_{3/2}$  and Co  $2p_{1/2}$  become visible. Presumably the transformation of the polymer film into a thin porous carbon shell results in shrinkage of the film, enabling the excited photoelectrons to pass through. Moreover, the main

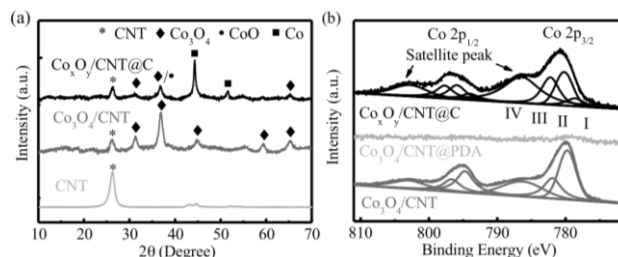


**Figure 2.** (a) X-ray diffraction patterns of commercially obtained CNTs,  $\text{Co}_3\text{O}_4/\text{CNT}$ s and  $\text{Co}_x\text{O}_y/\text{CNT}@C$ ; (b) XPS spectra of Co 2p of  $\text{Co}_3\text{O}_4/\text{CNT}$ s,  $\text{Co}_3\text{O}_4/\text{CNT}@PDA$  and  $\text{Co}_x\text{O}_y/\text{CNT}@C$ . I, II III and IV correspond to  $2p_{3/2}$  of Co metal,  $2p_{3/2}$  of  $\text{Co(II)O}$ ,  $2p_{3/2}$  of  $\text{Co(III)}$  and the satellite of Co  $2p_{3/2}$ , respectively.

spin orbit splitting components of Co 2p shifted slightly towards higher binding energies and two shake-up satellite peaks became more pronounced. This indicates that the oxidation state of the nanoparticles has changed and a fraction of the material became CoO, or even partly metallic Co [40–42]. In-situ experiments where samples were annealed and measured inside the XPS chamber without exposure to air, were also performed to study the evolution of the elements during annealing (Figure S5 and S6). For the sample in absence of PDA ( $\text{Co}_3\text{O}_4/\text{CNT}$ ), we observed intermediate CoO components after heating at  $400^\circ\text{C}$  (Figure S6). This also confirms that heating of  $\text{Co}_3\text{O}_4$  will release some oxygen from the oxide and convert it into CoO, and finally into Co, as observed from XRD.

For characterizing the electro-catalytic ORR properties of the synthesized samples in  $\text{N}_2$ - or  $\text{O}_2$ -saturated 0.1 M KOH solution cyclic voltammetry (CV) was applied. All the synthesized samples showed a quasi-rectangular double-layer capacity in  $\text{N}_2$ , and a well-defined ORR peak in presence of  $\text{O}_2$  (Figure 3a). For  $\text{Co}_x\text{O}_y/\text{CNT}@C$ , the cathodic peak located at 0.77V was more positive than that of  $\text{Co}_x\text{O}_y/\text{CNT}$  (0.74V) and  $\text{CNT}@C$  (0.67 V). To study the ORR kinetics of the synthesized sample, Koutecky-Levich plots ( $J^{-1}$  vs.  $\omega^{-1/2}$ ) were derived from Rotation Disk Electrode (RDE) measurements at various potentials, as shown in Figure 3b-d. The K-L plots show great linearity for all the samples, and the near parallelism of the fitting lines suggests two important points: i) clear first-order reaction kinetics with respect to the oxygen concentration and ii) similar electron transfer number for the ORR at various potentials. From the slopes we calculated the

electron transfer numbers to be 3.1 and 3.8 for  $\text{Co}_x\text{O}_y/\text{CNT}$  and  $\text{CNT}@\text{C}$  (inset of Figure 3b and c), and 4.0 for  $\text{Co}_x\text{O}_y/\text{CNT}@\text{C}$  (inset of Figure 3d). The latter value indicates an ideal reduction of  $\text{O}_2$  to  $\text{OH}^-$  instead of  $\text{HO}_2^-$ , which is also the case with the commercial  $\text{Pt}/\text{C}$  catalyst (Figure S7). Figure 3e shows that  $\text{Co}_x\text{O}_y/\text{CNT}@\text{C}$  has a more positive onset potential and higher cathodic current than  $\text{Co}_x\text{O}_y/\text{CNT}$  and  $\text{CNT}@\text{C}$ . For values below 0.6 V it is quite similar to commercial  $\text{Pt}/\text{C}$  (20%), although the cathodic peak position in the CV of  $\text{Co}_x\text{O}_y/\text{CNT}@\text{C}$  is slightly lower than that of  $\text{Pt}/\text{C}$  in Figure 3a. The Tafel slope of 58 mV/decade for  $\text{Co}_x\text{O}_y/\text{CNT}@\text{C}$  at a low over potential (Figure 3f) is much lower than that of  $\text{Co}_x\text{O}_y/\text{CNT}$  (93 mV/decade) and  $\text{CNT}@\text{C}$  (75 mV/decade), and even lower than that of  $\text{Pt}/\text{C}$  (62 mV/decade), showing promise as an alternative catalyst for ORR.

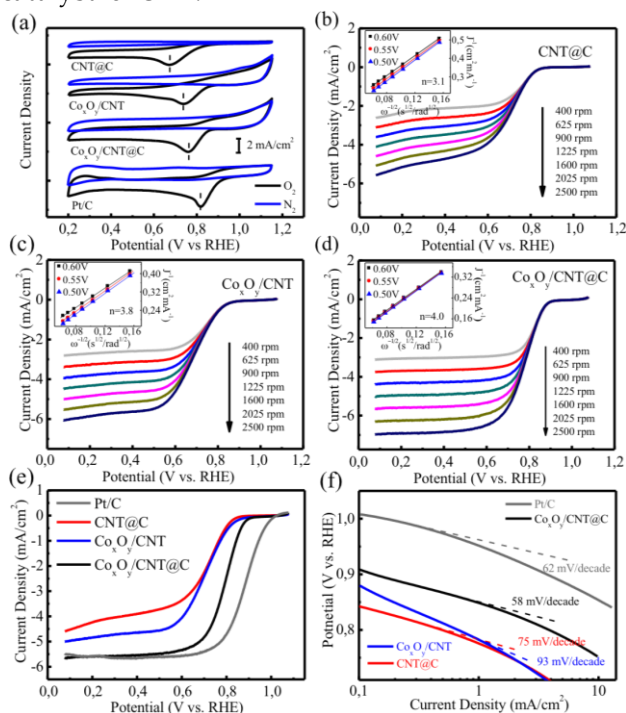


**Figure 3.** (a) CV curves of  $\text{CNT}@\text{C}$ ,  $\text{Co}_x\text{O}_y/\text{CNT}$  and  $\text{Co}_x\text{O}_y/\text{CNT}@\text{C}$  samples on glassy carbon in  $\text{O}_2$ -saturated (black line) or  $\text{N}_2$ -saturated (blue line) 0.1 M KOH solution at a scanning rate of 50 mV/s. Rotating-disk voltammetric profiles of (b)  $\text{CNT}@\text{C}$ , (c)  $\text{Co}_x\text{O}_y/\text{CNT}$  and (d)  $\text{Co}_x\text{O}_y/\text{CNT}@\text{C}$  in  $\text{O}_2$ -saturated 0.1 M KOH with a sweep rate of 10 mV/s at various rotation rates ranging from 400 rpm to 2500 rpm. The insets show the corresponding Koutecky–Levich plots at different potentials. (e) Rotating-Disk Electrode LSV curves of  $\text{CNT}@\text{C}$ ,  $\text{Co}_x\text{O}_y/\text{CNT}$ ,  $\text{Co}_x\text{O}_y/\text{CNT}@\text{C}$  and  $\text{Pt}/\text{C}$  in  $\text{O}_2$ -saturated 0.1 M KOH with a sweep rate of 10 mV/s at 1600 rpm. (f) Tafel plots of  $\text{CNT}@\text{C}$ ,  $\text{Co}_x\text{O}_y/\text{CNT}$ ,  $\text{Co}_x\text{O}_y/\text{CNT}@\text{C}$  and  $\text{Pt}/\text{C}$  derived by the mass-transport correction of corresponding RDE data.

The remaining question is related to the reason for the excellent activity of  $\text{Co}_x\text{O}_y/\text{CNT}@\text{C}$ . In some of the previously reported catalyst systems [43–46], the formation of Co-N bonding was proposed to greatly contribute to the ORR catalytic reactivity. However by comparing N 1s and Co 2p peaks of  $\text{CNT}@\text{PDA}$  and  $\text{Co}_3\text{O}_4/\text{CNT}@\text{PDA}$  at different annealing stages in Figure S8a and b, we see that both  $\text{CNT}@\text{PDA}$  and  $\text{Co}_3\text{O}_4/\text{CNT}@\text{PDA}$  at room temperature have a clear N 1s peak corresponding to the pyrrolic N in the polymer. After annealing at 600 °C, the content and ratio of pyrrolic, piridinic and quaternary N for  $\text{CNT}@\text{C}$  and  $\text{Co}_x\text{O}_y/\text{CNT}@\text{C}$  are almost the same, indicating that the  $\text{Co}_3\text{O}_4$  nanoparticles do not affect the evolution of the N during annealing. Also observable from Figure S8c is that the Co 2p peak exhibits almost the same shape and content in both  $\text{Co}_x\text{O}_y/\text{CNT}$  and  $\text{Co}_x\text{O}_y/\text{CNT}@\text{C}$  after annealing at 600 °C. This further indicates that the polydopamine polymer does not affect the evolution of Co. Therefore, we conclude that Co and N do not interact with each other during annealing, as no obvious formation of Co-N can be observed. This may be related to the fact that the polymer film is very thin and the total N content is very low, which is in contrast to other studies, where more bulky materials are used [43–46]. On the other hand, the density and size of the nanoparticles greatly affect the ORR catalytic activity. In Figure S9, samples with 100 applied ALD cycles show a low particle density, while after 500 applied ALD cycles the particles seriously increased in size. Both mentioned samples have lower activity compared to the sample with 300 cycles. Furthermore, with too high annealing temperatures, the nanoparticles grew into large particles (Figure S10), which also negatively affects the ORR activity. We thus conclude that the  $\text{Co}_x\text{O}_y$  nanoparticles embedded in the carbon shell are likely to be the main active component for the ORR in our case. Similar unintended results were shown in previous works [47–49]. The N-doped carbon shell resulting from the PDA pyrolysis is rather supportive in terms of facilitating an easier electron transfer between the embedded  $\text{Co}_x\text{O}_y$  nanoparticles and the electrode during the catalytic process [50,51], confirmed by impedance measurements in Figure S11.

Comparing to previous work on similar material

systems (Table S1), our composite shows the highest cathodic current density and lowest Tafel slope, indicating a successful approach towards improved ORR catalysts. The uniform distribution of the active  $\text{Co}_x\text{O}_y$  nanoparticles in both position and size assures the full utilization of the material for ORR, gaining more activity per mass. This uniformity is a direct result of atomic layer deposition, which deposits ideal  $\text{Co}_3\text{O}_4$  seeds, while the PDA hinders the  $\text{Co}_x\text{O}_y$  growth through Oswald ripening during the thermal annealing process (Figure 4a and c).

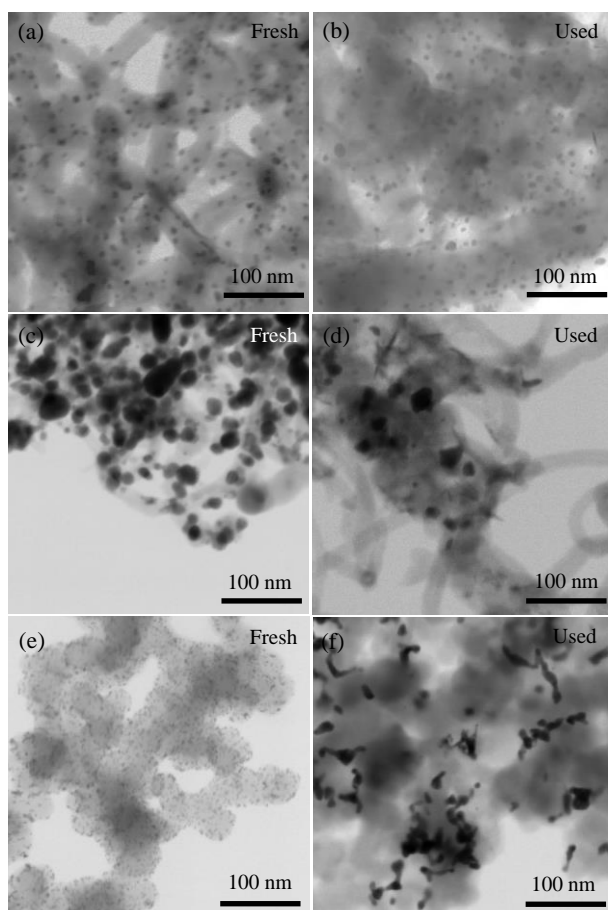


**Figure 4.** STEM images of  $\text{Co}_x\text{O}_y/\text{CNT}@C$  (a) as synthesized, (b) after 10000 testing cycles, and  $\text{Co}_x\text{O}_y/\text{CNT}$  (c) as synthesized, (d) after 10000 testing cycles; Pt/C (e) initial, (f) after 10000 testing cycles.

The stability/durability of the ORR catalyst is a further key issue besides the activity. It is commonly accepted that the instability of an ORR catalyst often originates from the agglomeration of the active nanoparticles (see commercial Pt/C before and after cycling in Figure 4e and f), or leaching of active

materials from the support (see  $\text{Co}_x\text{O}_y/\text{CNT}$  before and after cycling in Figure 4c and d). However,

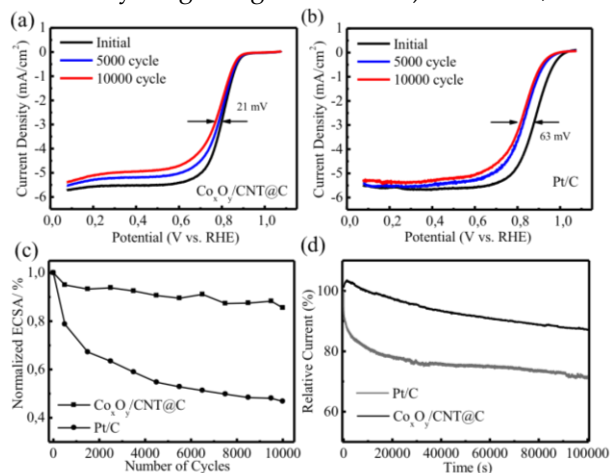


**Figure 5.** ORR curves of (a)  $\text{Co}_x\text{O}_y/\text{CNT}@C$  and (b) Pt/C samples in  $\text{O}_2$ -saturated 0.1 M KOH solution with a sweep rate of 10 mV/s at 1600 rpm over stability tests. (c) Loss of electrochemical surface area (ECSA) of  $\text{Co}_x\text{O}_y/\text{CNT}@C$  and Pt/C catalysts as a function of cycling numbers. (d) Current-time chronoamperometric-responses of  $\text{Co}_x\text{O}_y/\text{CNT}@C$  and Pt/C at 0.65 V (vs RHE.) in  $\text{O}_2$ -saturated 0.1 M KOH.

thanks to the PDA coating and the resulting embedding of the particles, the nano-architecture of  $\text{Co}_x\text{O}_y/\text{CNT}@C$ , including the size and density of the  $\text{Co}_x\text{O}_y$  particles, was perfectly maintained even after 10000 testing cycles (Figure 4a and b). Upon functional testing of the  $\text{Co}_x\text{O}_y/\text{CNT}@C$  sample, this is further reflected in the exceptional durability over extended CV cycling periods as well as the high stability, maintaining great performance at constant potential conditions, as clearly observed in Figure 5. The tests were carried out in  $\text{O}_2$ -saturated 0.1 M KOH for 10000 cycles. The half wave potential for  $\text{Co}_x\text{O}_y/\text{CNT}@C$  negatively shifted by 10 mV after 5000 cycles towards 21 mV after 10000 cycles (Figure 5a), which is considerably lower than the values obtained from the commercial Pt/C sample, namely 50 mV and 63 mV, respectively (Figure 5b). Furthermore, the  $\text{Co}_x\text{O}_y/\text{CNT}@C$  catalyst lost only about 14% of its initial electrochemical surface area (ECSA) after 10000 test cycles, while the ECSA of Pt/C decreased by 65% after the same number of cycles (Figure 5c). The stability of the  $\text{Co}_x\text{O}_y/\text{CNT}@C$  catalyst was further characterized by chrono-amperometry. Figure 5d shows that after 100000 s the current was still at 83% of the initial value, corresponding to a loss of only 17%. Note that the Pt/C reference sample showed a loss of 35% in identical conditions. Figure S12 shows

that the XPS spectra of the Co 2p and N1s are almost identical before and after the test. This suggests that the Co becomes slightly oxidized while the N atoms remain the same even after long-term testing, confirming exceptional stability and durability.

We conclude that this outstanding stability/durability is likely to be related to the embedding of the nanoparticles into the coating during the composite formation. The pyrolysis-derived carbon shell not only prevented the nanoparticles from detaching off of the CNT but also minimized the mobility of the nanoparticles as in Figure 4a and b. While in Figure S12, the XPS spectra for both Co 2p and N 1s peak of the  $\text{Co}_x\text{O}_y/\text{CNT}@C$  sample show slight changes before and after the cycling tests. Therefore the architecture of the  $\text{Co}_x\text{O}_y/\text{CNT}@C$  is greatly preserved as well as the electronic states of the materials due to the embedding concept, which is resulting in an exceptional stability/durability. Comparing to further work with similar material systems (Table S1), the  $\text{Co}_x\text{O}_y/\text{CNT}@C$  are among the most stable/durable for the longest testing durations, showing the intended coating of N-doped carbon shell is a true benefit for maintaining the reactivity over long-term operation.

## 4 Conclusions

In summary, we have demonstrated a very elegant method to fabricate highly dispersed  $\text{Co}_x\text{O}_y$  nanoparticles embedded in a carbon matrix, which as final composite acts as very efficient non-noble metal catalyst for the ORR reaction. Nanoparticles of  $\text{Co}_x\text{O}_y$  are grown on defect sites of CNTs by ALD in a very controlled size distribution and a doped carbon shell is obtained after subsequent coating with PDA and its pyrolysis. This formed carbon film has proven to be an effective way to prevent agglomeration and leaching of the nanoparticles while at the same time having a positive impact on the reactivity of the composite for the ORR. Moreover, it is likely that such a conductive coating is supportive for the catalytic reaction through enhancing the electron transfer rate. Owing to this unique architecture, the synthesized samples show much higher stability and durability than the commonly applied commercial Pt/C catalyst, offering a great opportunity to substitute noble metal catalysts in emerging energy-related applications. This proposed design is

not specific for the described problem, but can be easily extended to the synthesis of further catalysts and sensors or other functional materials.

## Acknowledgements

The authors acknowledge financial support by the Spanish ministry of economy and competitiveness (MINECO) through project numbers MAT2012-38161 and MAT2013-46593-C6 and the Basque government through project numbers PI2013-56 and Grant IT-621-13. M.K. acknowledges financial support through Marie Curie Actions (CIG) within project number 322158 (ARTEN). The authors also want to thank Dr. Jens Brede for the helpful discussions.

**Electronic Supplementary Material:** Supplementary material (SEM, EDX, XRD and XPS profile of  $\text{Co}_3\text{O}_4/\text{CNT}$  and  $\text{Co}_3\text{O}_4/\text{CNT}@C$ ; RRDE response of Pt/C,  $\text{Co}_3\text{O}_4/\text{CNT}$  and  $\text{Co}_3\text{O}_4/\text{CNT}@C$ ) is available in the online version of this article at (automatically inserted by the publisher).

## References

- [1] Rabis, A.; Rodriguez, P.; Schmidt, T. J. Electrocatalysis for Polymer Electrolyte Fuel Cells: Recent Achievements and Future Challenges. *ACS Catal.* **2012**, *2*, 864–890
- [2] Zhang, S.; Shao, Y.; Yin, G.; Lin, Y. Recent Progress in Nanostructured Electrocatalysts for PEM Fuel Cells. *J. Mater. Chem. A* **2013**, *1*, 4631–4641.
- [3] Katsounaros, I.; Cherevko, S.; Zeradjanin, A. R.; Mayrhofer, K. J. J. Oxygen Electrochemistry as a Cornerstone for Sustainable Energy Conversion. *Angew. Chem. Int. Ed. Engl.* **2014**, *53*, 102–121.
- [4] Stephens, I. E. L.; Bondarenko, A. S.; Grønbjerg, U.; Rossmeisl, J.; Chorkendorff, I. Understanding the Electrocatalysis of Oxygen Reduction on Platinum and Its Alloys. *Energy Environ. Sci.* **2012**, *5*, 6744–6762.
- [5] Guo, S.; Zhang, S.; Sun, S. Tuning Nanoparticle Catalysis for the Oxygen Reduction Reaction. *Angew. Chem. Int. Ed. Engl.* **2013**, *52*, 8526–8544.
- [6] Wu, J.; Yang, H. Platinum-Based Oxygen Reduction Electrocatalysts. *Acc. Chem. Res.* **2013**, *46*, 1848–1857.

- [7] Zhou, X.; Qiao, J.; Yang, L.; Zhang, J. A Review of Graphene-Based Nanostructural Materials for Both Catalyst Supports and Metal-Free Catalysts in PEM Fuel Cell Oxygen Reduction Reactions. *Adv. Energy Mater.* **2014**, *4*, 1301523.
- [8] Wang, D.-W.; Su, D. Heterogeneous Nanocarbon Materials for Oxygen Reduction Reaction. *Energy Environ. Sci.* **2014**, *7*, 576–591.
- [9] Yao, Y.; You, Y.; Zhang, G.; Liu, J.; Sun, H.; Zou, Z.; Sun, S. Highly Functional Bioinspired Fe/N/C Oxygen Reduction Reaction Catalysts: Structure-Regulating Oxygen Sorption. *ACS Appl. Mater. Interfaces* **2016**, *8*, 6464–6471.
- [10] Zhang, J.; Chen, G.; Zhang, Q.; Kang, F.; You, B. Self-Assembly Synthesis of N-Doped Carbon Aerogels for Supercapacitor and Electrocatalytic Oxygen Reduction. *ACS Appl. Mater. Interfaces* **2015**, *7*, 12760–12766.
- [11] Wu, Z.; Yang, S.; Sun, Y.; Parvez, K.; Feng, X.; Müllen, K. 3D Nitrogen-Doped Graphene Aerogel-Supported Fe<sub>3</sub>O<sub>4</sub> Nanoparticles as Efficient Electrocatalysts for the Oxygen Reduction Reaction. *J. Am. Chem. Soc.* **2012**, *134*, 9082–9085.
- [12] Zang, Y.; Zhang, H.; Zhang, X.; Liu, R.; Liu, S.; Wang, G.; Zhang, Y.; Zhao, H. Fe/Fe<sub>2</sub>O<sub>3</sub> nanoparticles anchored on Fe-N-doped carbon nanosheets as bifunctional oxygen electrocatalysts for rechargeable zinc-air batteries. *Nano Res.* **2016**, *9*, 2123–2137.
- [13] Liang, Y.; Li, Y.; Wang, H.; Zhou, J.; Wang, J.; Regier, T.; Dai, H. Co<sub>3</sub>O<sub>4</sub> Nanocrystals on Graphene as a Synergistic Catalyst for Oxygen Reduction Reaction. *Nat. Mater.* **2011**, *10*, 780–786.
- [14] Ren, G.; Li, Y.; Guo, Z.; Xiao, G.; Zhu, Y.; Dai, L.; Jiang, L. A bio-inspired Co<sub>3</sub>O<sub>4</sub>-polypyrrole-graphene complex as an efficient oxygen reduction catalyst in one-step ball milling. *Nano Res.* **2015**, *8*, 3461–3471.
- [15] Liang, Y.; Wang, H.; Diao, P.; Chang, W.; Hong, G.; Li, Y.; Gong, M.; Xie, L.; Zhou, J.; Wang, J.; Regier, T. Z.; Wei, F.; Dai, H. Oxygen Reduction Electrocatalyst Based on Strongly Coupled Cobalt Oxide Nanocrystals and Carbon Nanotubes. *J. Am. Chem. Soc.* **2012**, *134*, 15849–15857.
- [16] Gao, R.; Li, Z.; Zhang, X.; Zhang, J.; Hu, Z.; Liu, X. Carbon-Dotted Defective CoO with Oxygen Vacancies: A Synergetic Design of Bifunctional Cathode Catalyst for Li–O<sub>2</sub> Batteries. *ACS Catal.* **2016**, *6*, 400–406.
- [17] Zhang, X.; Gao, R.; Li, Z.; Hu, Z.; Liu, H.; Liu, X. Enhancing the Performance of CoO as Cathode Catalyst for Li–O<sub>2</sub> Batteries through Confinement into Bimodal Mesoporous Carbon. *Electrochim. Acta.* **2016**, *201*, 134–141.
- [18] Jin, H.; Wang, J.; Su, D.; Wei, Z.; Pang, Z.; Wang, Y. In situ cobalt-cobalt oxide/N-doped carbon hybrids as superior bifunctional electrocatalysts for hydrogen and oxygen evolution. *J. Am. Chem. Soc.* **2015**, *137*, 2688–94.
- [19] Monzon, L. M. A.; Rode, K.; Venkatesan, M.; Coey, J. M. D. Electrosynthesis of Iron, Cobalt, and Zinc Microcrystals and Magnetic Enhancement of the Oxygen Reduction Reaction. *Chem. Mater.* **2012**, *24*, 3878–3885.
- [20] Zhang, T.; Cheng, F.; Du, J.; Hu, Y.; Chen, J. Efficiently Enhancing Oxygen Reduction Electrocatalytic Activity of MnO<sub>2</sub> Using Facile Hydrogenation. *Adv. Energy Mater.* **2015**, *5*, 1400654.
- [21] Sun, M.; Dong, Y.; Zhang, G.; Qu, J.; Li, J.  $\alpha$ -Fe<sub>2</sub>O<sub>3</sub> Spherical Nanocrystals Supported on CNTs as Efficient Non-Noble Electrocatalysts for the Oxygen Reduction Reaction. *J. Mater. Chem. A* **2014**, *2*, 13635–13640.
- [22] Zhang, G.; Xia, B. Y.; Wang, X.; David Lou, X. W. Strongly Coupled NiCo<sub>2</sub>O<sub>4</sub>-rGO Hybrid Nanosheets as a Methanol-Tolerant Electrocatalyst for the Oxygen Reduction Reaction. *Adv. Mater.* **2014**, *26*, 2408–2412.
- [23] Lv, L.-B.; Ye, T.-N.; Gong, L.-H.; Wang, K.-X.; Su, J.; Li, X.-H.; Chen, J.-S. Anchoring Cobalt Nanocrystals through the Plane of Graphene: Highly Integrated Electrocatalyst for Oxygen Reduction Reaction. *Chem. Mater.* **2015**, *27*, 544–549.
- [24] Bag, S.; Roy, K.; Gopinath, C. S.; Raj, C. R. Facile Single-Step Synthesis of Nitrogen-Doped Reduced Graphene Oxide-Mn<sub>3</sub>O<sub>4</sub> Hybrid Functional Material for

- the Electrocatalytic Reduction of Oxygen. *ACS Appl. Mater. Interfaces* **2014**, *6*, 2692–2699.
- [25] Feng, J.; Liang, Y.; Wang, H.; Li, Y.; Zhang, B.; Zhou, J.; Wang, J.; Regier, T.; Dai, H. Engineering manganese oxide/nanocarbon hybrid materials for oxygen reduction electrocatalysis, *Nano Res.* **2012**, *5*, 718–725.
- [26] Banham, D.; Ye, S.; Pei, K.; Ozaki, J.; Kishimoto, T.; Imashiro, Y. A Review of the Stability and Durability of Non-Precious Metal Catalysts for the Oxygen Reduction Reaction in Proton Exchange Membrane Fuel Cells. *J. Power Sources* **2015**, *285*, 334–348.
- [27] Pinna, N.; Knez, M. *Atomic Layer Deposition of Nanostructured Materials*; Wiley-VCH: Weinheim, Germany, 2011.
- [28] Knez, M.; Nielsch, K.; Niinistö, L. Synthesis and Surface Engineering of Complex Nanostructures by Atomic Layer Deposition. *Adv. Mater.* **2007**, *19*, 3425–3438.
- [29] Tong, X.; Qin, Y.; Guo, X.; Moutanabbir, O.; Ao, X.; Pippel, E.; Zhang, L.; Knez, M. Enhanced Catalytic Activity for Methanol Electro-Oxidation of Uniformly Dispersed Nickel Oxide Nanoparticles-Carbon Nanotube Hybrid Materials. *Small* **2012**, *8*, 3390–3395.
- [30] Yang, F.; Zhang, L.; Zuzuarregui, A.; Gregorczyk, K.; Li, L.; Beltrán, M.; Tollan, C.; Brede, J.; Rogero, C.; Chuvilin, A.; Knez, M. Functionalization of Defect Sites in Graphene with RuO<sub>2</sub> for High Capacitive Performance. *ACS Appl. Mater. Interfaces* **2015**, *7*, 20513–20519.
- [31] Puurunen, R. L.; Vandervorst, W. Island Growth as a Growth Mode in Atomic Layer Deposition: A Phenomenological Model. *J. Appl. Phys.* **2004**, *96*, 7686–7695.
- [32] Lee, H.; Dellatore, S. M.; Miller, W. M.; Messersmith, P. B. Mussel-Inspired Surface Chemistry for Multifunctional Coatings. *Science* **2007**, *318*, 426–430.
- [33] Fei, B.; Qian, B.; Yang, Z.; Wang, R.; Liu, W. C.; Mak, C. L.; Xin, J. H. Coating Carbon Nanotubes by Spontaneous Oxidative Polymerization of Dopamine. *Carbon* **2008**, *46*, 1795–1797.
- [34] Liu, Y.; Ai, K.; Lu, L. Polydopamine and Its Derivative Materials: Synthesis and Promising Applications in Energy, Environmental, and Biomedical Fields. *Chem. Rev.* **2014**, *114*, 5057–5115.
- [35] Malecki, A.; Tareen, J. A. K.; Doumerc, J. P.; Rabardel, L.; Launay, J. C. Kinetics of Thermal Decomposition of Co<sub>3</sub>O<sub>4</sub> Powder and Single Crystals. *J. Solid State Chem.* **1985**, *57*, 49–57.
- [36] Malecki, A.; Doumerc, J. P. Kinetics of Thermal Decomposition of Co<sub>3</sub>O<sub>4</sub> the Kinetic Model. *J. Therm. Anal.* **1990**, *36*, 215–222.
- [37] Toniolo, J. C.; Takimi, A. S.; Bergmann, C. P. Nanostructured Cobalt Oxides (Co<sub>3</sub>O<sub>4</sub> and CoO) and Metallic Co Powders Synthesized by the Solution Combustion Method. *Mater. Res. Bull.* **2010**, *45*, 672–676.
- [38] Domínguez, M.; Taboada, E.; Idriss, H.; Molins, E.; Llorca, J. Fast and efficient hydrogen generation catalyzed by cobalt talc nanolayers dispersed in silica aerogel. *J. Mater. Chem.* **2010**, *20*, 4875–4883.
- [39] Ho, C.; Weng, T.; Wang, C.; Yen, S.; Yew, T. Tunable band gaps of Co<sub>3-x</sub>Cu<sub>x</sub>O<sub>4</sub> nanorods with various Cu doping concentrations. *RSC Adv.* **2014**, *4*, 20053–20057.
- [40] Petitto, S. C.; Marsh, E. M.; Carson, G. A.; Langel, M. A. Cobalt Oxide Surface Chemistry: The Interaction of CoO(100), Co<sub>3</sub>O<sub>4</sub>(110) and Co<sub>3</sub>O<sub>4</sub>(111) with Oxygen and Water. *J. Mol. Catal. A Chem.* **2008**, *281*, 49–58.
- [41] Cui, J.; Zhang, X.; Tong, L.; Luo, J.; Wang, Y.; Zhang, Y.; Xie, K.; Wu, Y. Facile Synthesis of Mesoporous Co<sub>3</sub>O<sub>4</sub>/CeO<sub>2</sub> Hybrid Nanowire Arrays for High Performance Supercapacitors. *J. Mater. Chem. A* **2015**, *3*, 10426–10431.
- [42] Qiao, L.; Xiao, H. Y.; Meyer, H. M.; Sun, J. N.; Rouleau, C. M.; Paretzky, A. A.; Geohegan, D. B.; Ivanov, I. N.; Yoon, M.; Weber, W. J.; *et al.* Nature of the Band Gap and Origin of the Electro-/photo-Activity of Co<sub>3</sub>O<sub>4</sub>. *J. Mater. Chem. C* **2013**, *1*, 4628–4633.
- [43] Wu, G.; More, K. L.; Johnston, C. M.; Zelenay, P. High-Performance Electrocatalysts for Oxygen Reduction Derived from Polyaniline, Iron, and Cobalt. *Science* **2011**, *332*, 443–447.

- [44] Bashyam, R.; Zelenay, P. A Class of Non-Precious Metal Composite Catalysts for Fuel Cells. *Nature* **2006**, *443*, 63–66.
- [45] Chao, S.; Cui, Q.; Bai, Z.; Yan, H.; Wang, K.; Yang, L. Varying N Content and N/C Ratio of the Nitrogen Precursor to Synthesize Highly Active Co-N<sub>x</sub>/C Non-Precious Metal Catalyst. *Int. J. Hydrogen Energy* **2014**, *39*, 14768–14776.
- [46] Huang, D.; Luo, Y.; Li, S.; Zhang, B.; Shen, Y.; Wang, M. Active catalysts based on cobalt oxide@cobalt/N-C nanocomposites for oxygen reduction reaction in alkaline solutions, *Nano Res.* **2014**, *7*, 1054–1064.
- [47] Xiao, M.; Zhu, J.; Feng, L.; Liu, C.; Xing, W. Meso/macroporous Nitrogen-Doped Carbon Architectures with Iron Carbide Encapsulated in Graphitic Layers as an Efficient and Robust Catalyst for the Oxygen Reduction Reaction in Both Acidic and Alkaline Solutions. *Adv. Mater.* **2015**, *27*, 2521–2527.
- [48] Wang, Z.; Li, B.; Ge, X.; Goh, F. W. T.; Zhang, X.; Du, G.; Wu, D.; Liu, Z.; Hor, T. S. A.; Zhang, H.; Zong, Y. Co@Co<sub>3</sub>O<sub>4</sub>@PPD Core@bshell Nanoparticle-Based Composite as an Efficient Electrocatalyst for Oxygen Reduction Reaction. *Small* **2016**, 1–8.
- [49] Li, Y.; Cheng, F.; Zhang, J.; Chen, Z.; Xu, Q.; Guo, S. Cobalt-Carbon Core-Shell Nanoparticles Aligned on Wrinkle of N-Doped Carbon Nanosheets with Pt-Like Activity for Oxygen Reduction. *Small* **2016**, *123*, 1–7.
- [50] Aijaz, A.; Masa, J.; Röler, C.; Xia, W.; Weide, P.; Botz, A. J. R.; Fischer, R. A.; Schuhmann, W.; Muhler, M. Co@Co<sub>3</sub>O<sub>4</sub> Encapsulated in Carbon Nanotube-Grafted Nitrogen-Doped Carbon Polyhedra as an Advanced Bifunctional Oxygen Electrode. *Angew. Chem. Int. Ed. Engl.* **2016**, *55*, 4087–4091.
- [51] Masa, J.; Xia, W.; Sinev, I.; Zhao, A.; Sun, Z.; Grütze, S.; Weide, P.; Muhler, M.; Schuhmann, W. Mn<sub>x</sub>O<sub>y</sub>/NC and Co<sub>x</sub>O<sub>y</sub>/NC Nanoparticles Embedded in a Nitrogen-Doped Carbon Matrix for High-Performance Bifunctional Oxygen Electrodes. *Angew. Chem. Int. Ed. Engl.* **2014**, *53*, 8508–8512.



## Electronic Supplementary Material

# Design of Active and Stable Oxygen Reduction Reaction Catalysts by Embedding $\text{Co}_x\text{O}_y$ Nanoparticles into Nitrogen-Doped Carbon

Fan Yang<sup>1</sup>, Mikel Abadia<sup>2</sup>, Chaoqiu Chen<sup>1</sup>, Weike Wang<sup>1</sup>, Le Li<sup>1</sup>, Lianbing Zhang<sup>1</sup> (✉), Celia Rogero<sup>2, 3</sup>, Andrey Chuvilin<sup>1, 4</sup>, and Mato Knez<sup>1, 4</sup> (✉)

<sup>1</sup>CIC nanoGUNE Consolider, Tolosa Hiribidea 76, 20018 Donostia-San Sebastian, Spain

<sup>2</sup>Centro de Física de Materials, Paseo Manuel de Lardizabal, 5, 20018 Donostia-San Sebastian, Spain

<sup>3</sup>Donostia International Physics Center (DIPC), Paseo Manuel de Lardizabal, 4, 20018 Donostia-San Sebastian, Spain

<sup>4</sup>IKERBASQUE, Basque Foundation for Science, Maria Diaz de Haro 3, 48013 Bilbao, Spain

Supporting information to DOI 10.1007/s12274-\*\*\*\*-\*\*\*\*-\* (automatically inserted by the publisher)

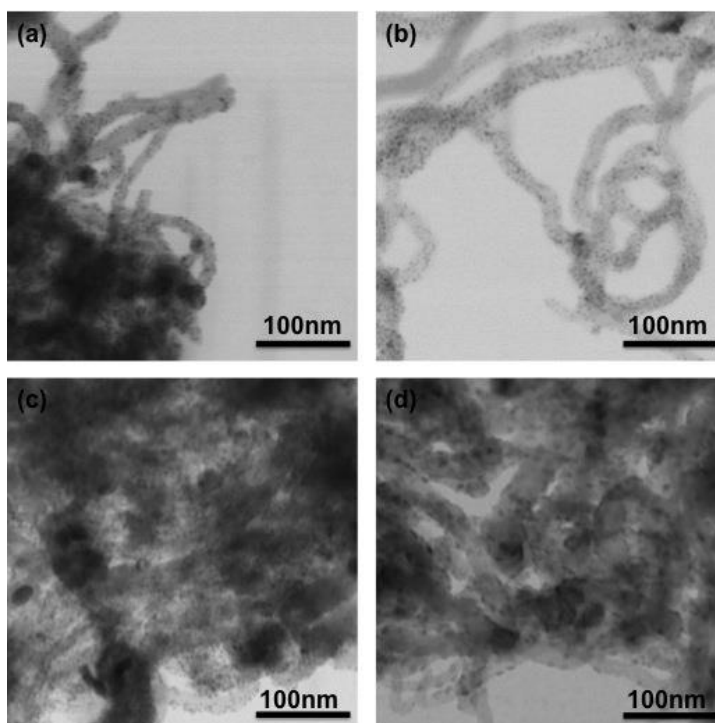


Fig. S1 in the Electronic Supplementary Material (ESM). STEM images of  $\text{Co}_3\text{O}_4$  nanoparticles grown on CNTs after various ALD cycle numbers, a) 100 cycles, b) 300 cycles, c) 500 cycles and d) 700 cycles.

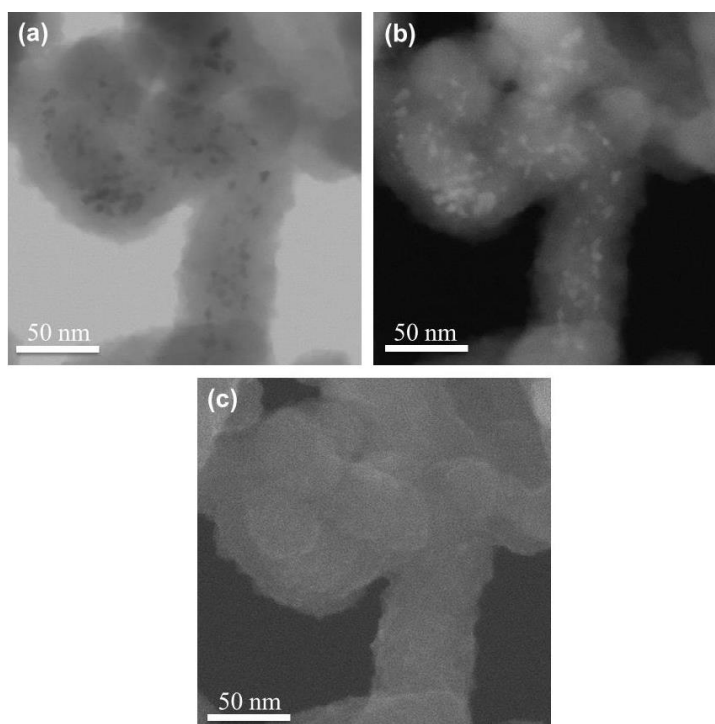


Fig. S2. STEM image of  $\text{Co}_3\text{O}_4/\text{CNT}@PDA$  (a) bright field, (b) dark field and (c) morphology.

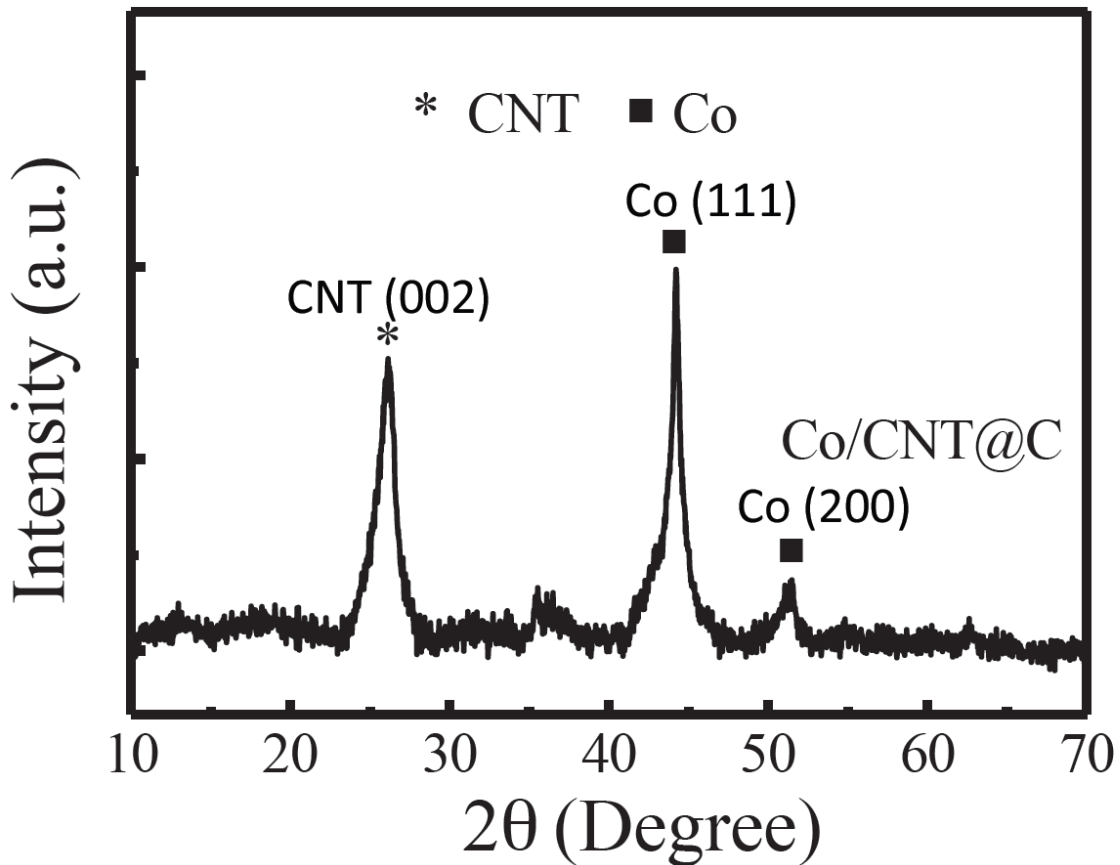


Figure S3. X-ray diffraction patterns of Co/CNT@C, obtained from  $\text{Co}_3\text{O}_4/\text{CNTs@PDA}$  after annealing at 800 °C.

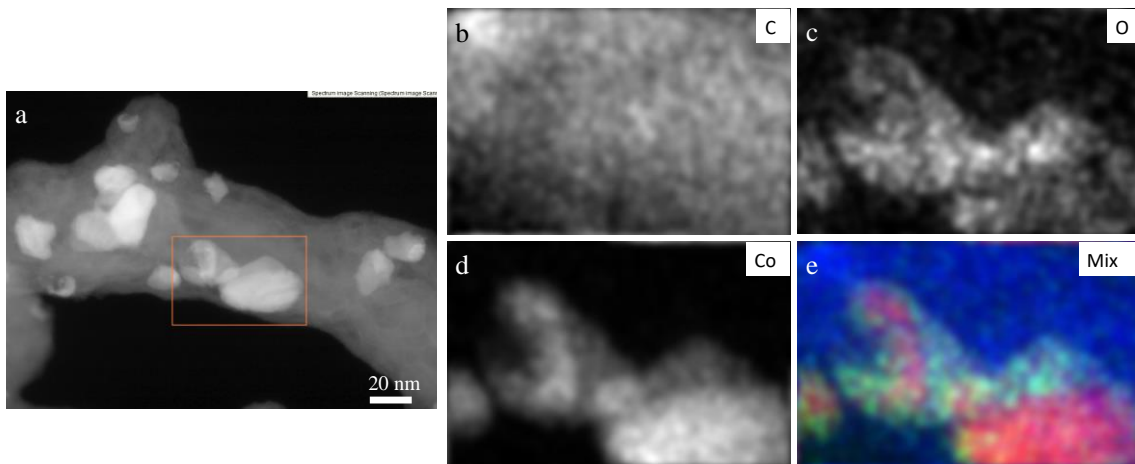


Figure S4 in ESM. Element analysis of  $\text{Co}_x\text{O}_y$  nanoparticles, (a) High-angle annular dark-field STEM image, (b)–(d) Elemental maps of the box area in (a) for (b) Carbon (C), (c) Oxygen (O) and (d) Cobalt (Co) and (e) mix of the elements: blue represents carbon, green represents oxygen and red represents cobalt.

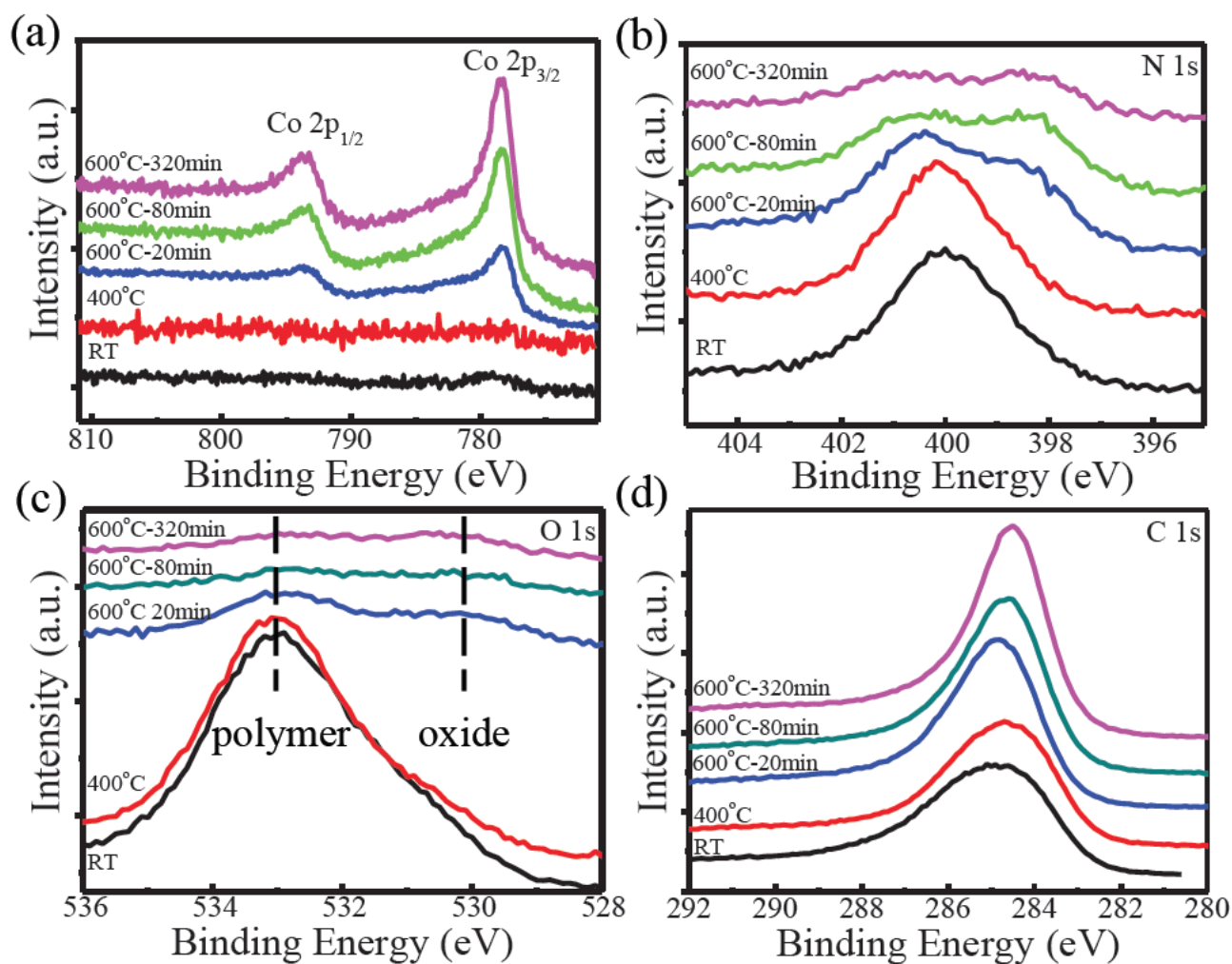


Figure S5. In-situ annealing of  $\text{Co}_3\text{O}_4/\text{CNTs}@PDA$  in the XPS chamber upon different annealing stages: Evolution of (a) Co 2p, (b) N 1s, (c) O 1s and (d) C 1s in the XPS spectra.

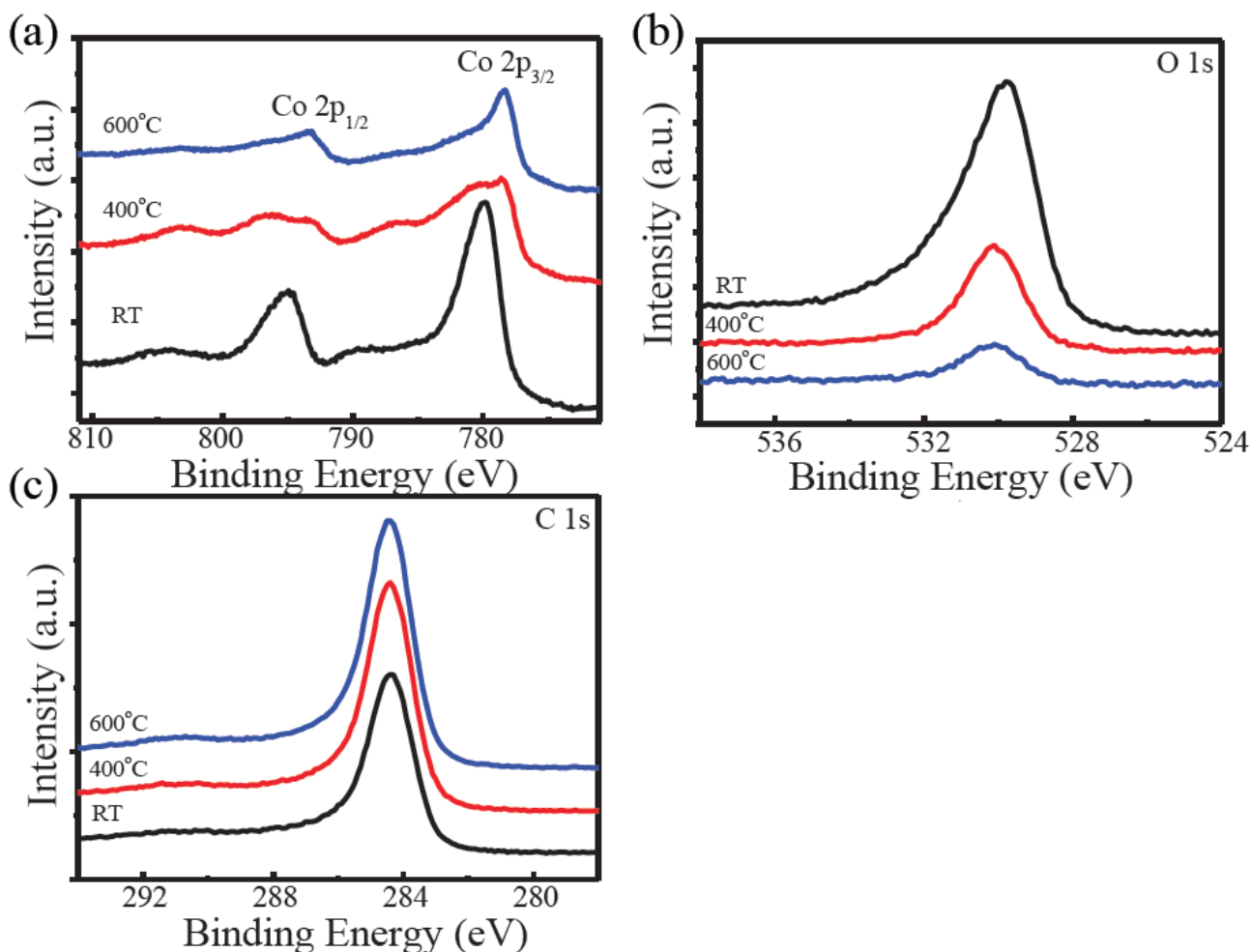


Figure S6. In-situ annealing of  $\text{Co}_3\text{O}_4/\text{CNTs}$  in the XPS chamber upon different annealing stages: Evolution of (a) Co 2p, (b) O 1s and (c) C 1s in the XPS spectrum. To demonstrate the reduction of the nanoparticles during annealing, we performed in-situ experiments where samples were annealed and measured inside the XPS chamber, i.e. in ultra high vacuum conditions. As shown in Figure S5a, Co 2p peaks were not observed until the sample was heated at 600 °C for 20 min. The shape and energy position of Co 2p core levels suggests that Co metal was already the dominant part at the surface of the nanoparticle. The spectrum of the sample without PDA coating showed the same tendency, but in this case we observed the intermediate CoO components after heating at 400 °C (Figure S6a). These results confirm that heating of  $\text{Co}_3\text{O}_4$  will release some oxygen from the oxide and convert it into CoO, and finally into Co metal, as also observed from XRD. XPS was applied to study the evolution of N, O and C, the constituting elements of PDA. Figure S5b shows that the intensity of the N 1s peak kept decreasing during annealing. After annealing at 600 °C for 20 min the pyrrolic N started converting into pyridinic N and quaternary N. The O 1s peak initially showed high intensity at 533.2 eV corresponding to the O from the PDA. During annealing the intensity decreased as the PDA kept releasing O and converting into carbon. Owing to the shrinkage of PDA, a new peak of O 1s at 530.4 eV occurred. This O stems from the cobalt oxide in the vicinity of the surface. Upon further annealing, the intensity of both O peaks decreased until they eventually vanished. The C 1s peak intensity steadily increased due to the formation of the carbon shell.

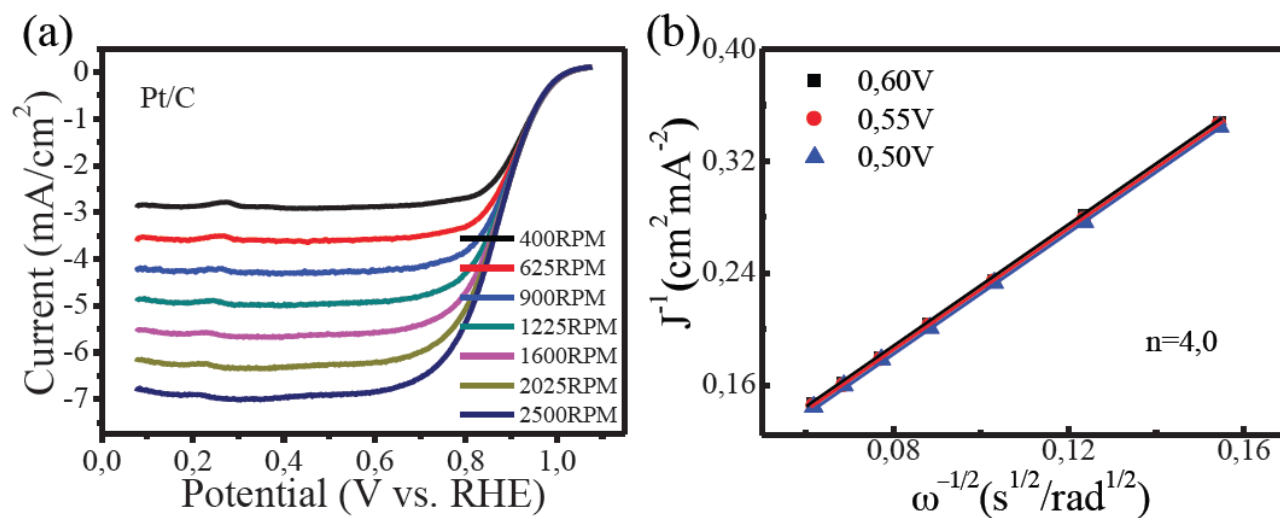


Figure S7. (a) Rotating-Disc Electrode voltammetric profiles of Pt/C in O<sub>2</sub>-saturated 0.1 M KOH with a sweep rate of 10 mV/s at the different rotation rates ranging from 400 rpm to 2500 rpm. (b) Koutecky–Levich plots at different potentials of Pt/C.

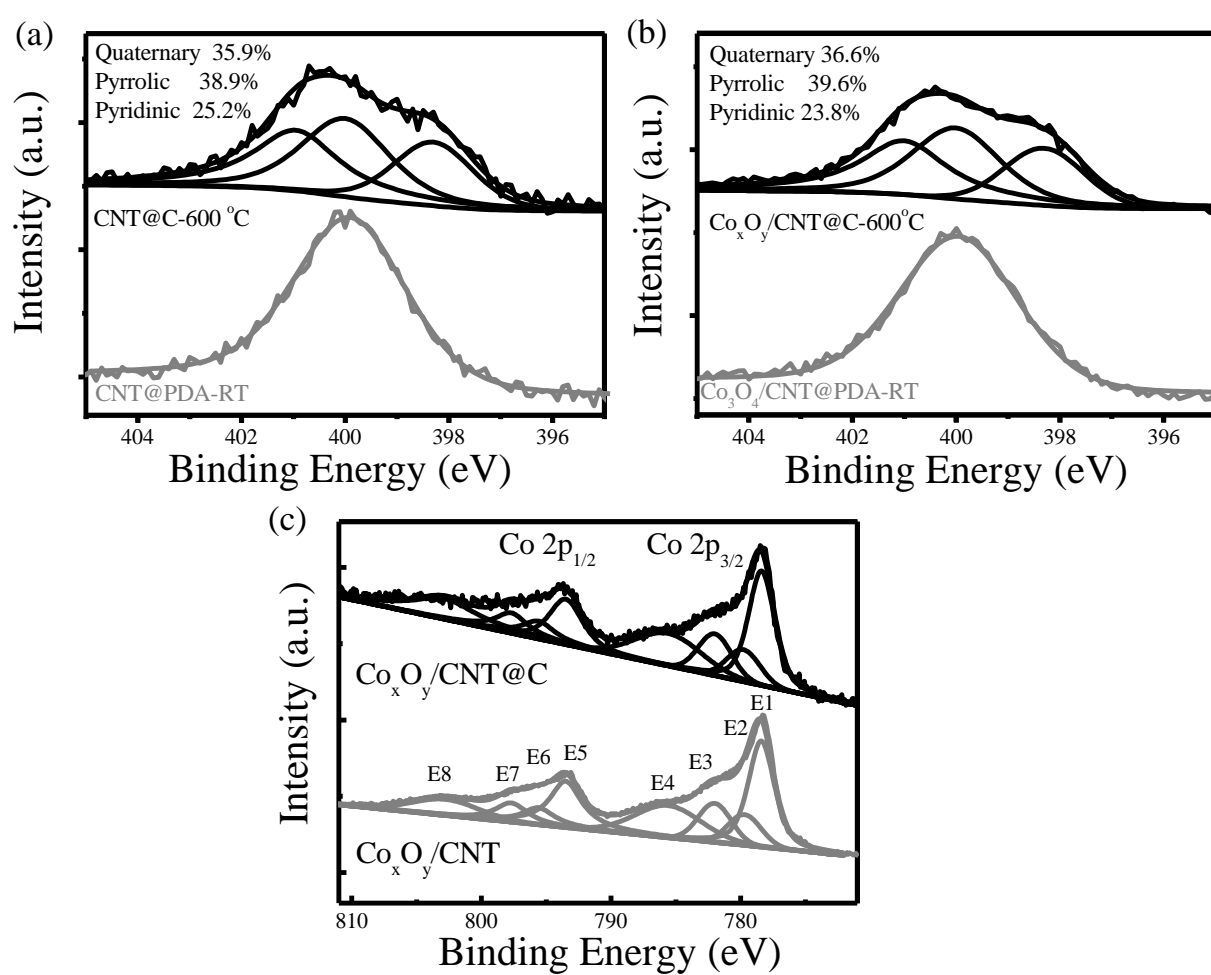


Figure S8. N 1s evolution before and after annealing at 600 °C in the XPS chamber with (a) CNT@PDA (b) Co<sub>3</sub>O<sub>4</sub>/CNTs@PDA, and (c) Co 2p evolution comparison of Co<sub>3</sub>O<sub>4</sub>/CNTs@PDA and CNT@PDA after annealing at 600 °C in the XPS chamber. E1-E8 corresponds to 2p<sub>3/2</sub> for Co metal, Co(II), Co (III), satellite of Co 2p<sub>3/2</sub>, 2p<sub>1/2</sub> for Co metal, Co(II), Co(III) and satellite of Co 2p<sub>1/2</sub>, respectively.

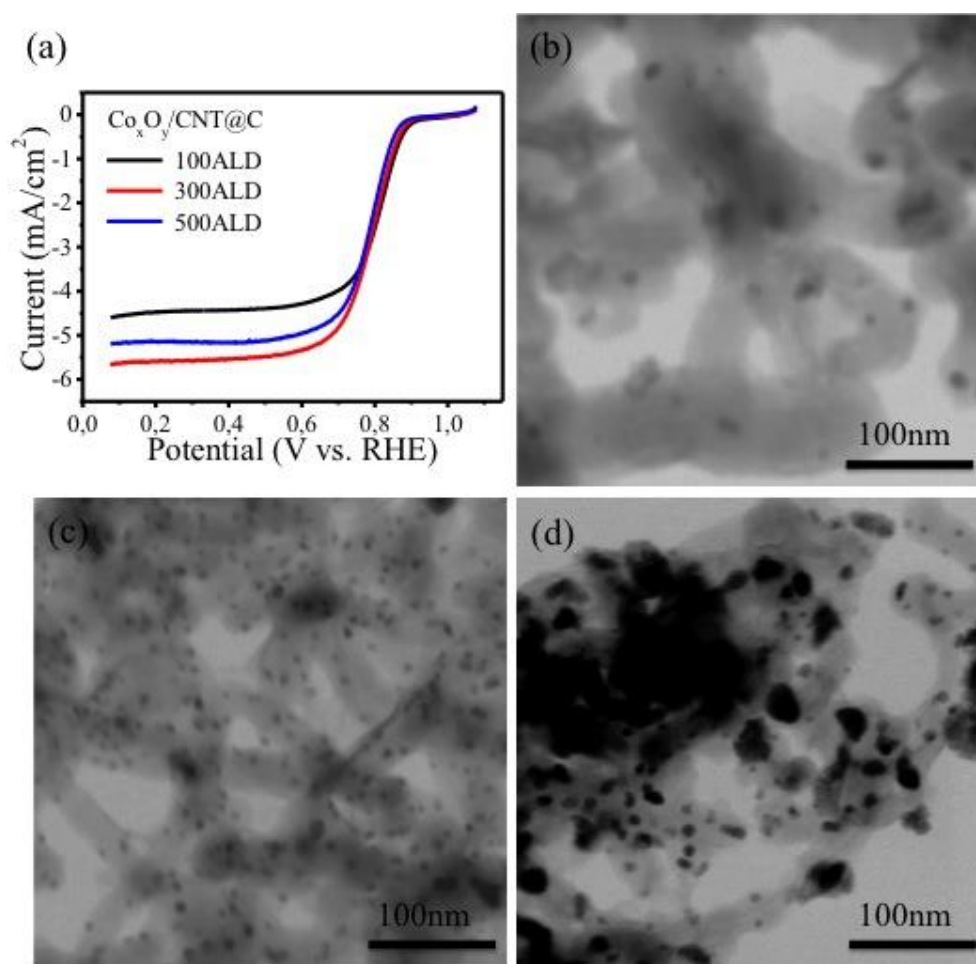


Figure S9. (a) Rotating-Disk Electrode LSV curves of Co<sub>x</sub>O<sub>y</sub>/CNT@C with various applied ALD cycles in O<sub>2</sub>-saturated 0.1M KOH with a sweep rate of 10 mV/s at 1600 rpm. STEM images of Co<sub>x</sub>O<sub>y</sub>/CNT@C with various applied ALD cycles (b) 100 cycles, (c) 300 cycles, (d) 500 cycles.

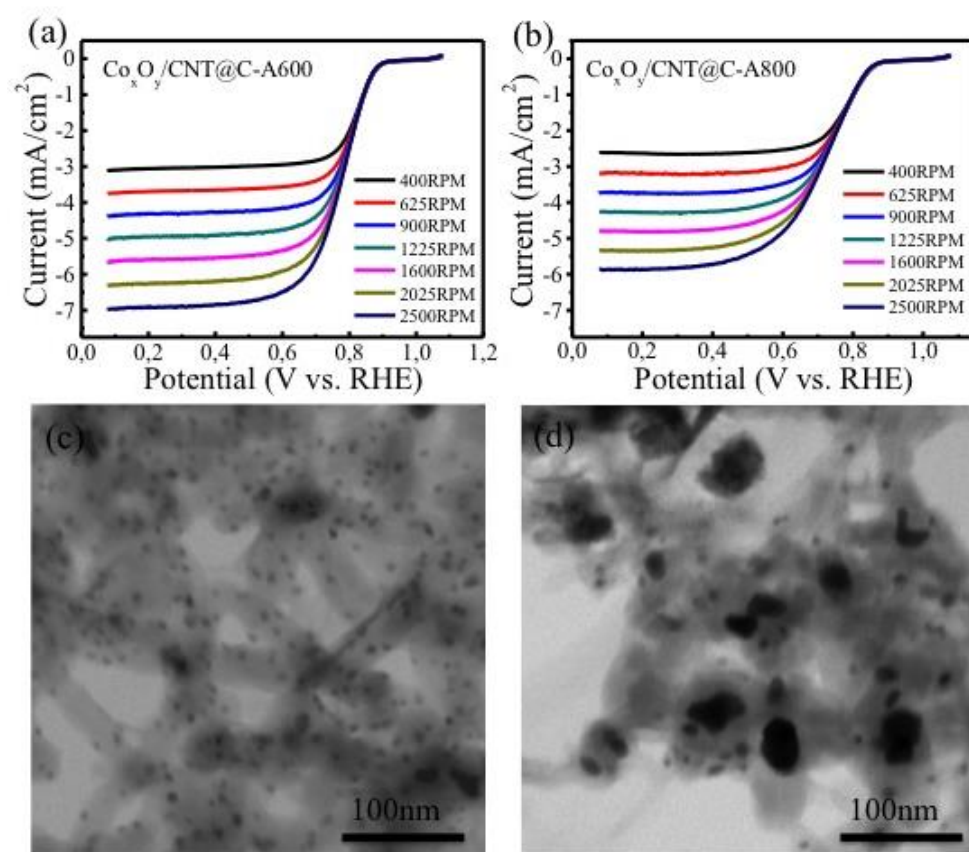


Figure S10. Rotating-Disk Electrode LSV curves of  $\text{Co}_x\text{O}_y/\text{CNT}@C$  annealed at various temperatures (a) 600 °C, (b) 800 °C in  $\text{O}_2$ -saturated 0.1 M KOH with a sweep rate of 10 mV/s at 1600 rpm. STEM images of  $\text{Co}_x\text{O}_y/\text{CNT}@C$  annealed at various temperatures (c) 600 °C, (d) 800 °C. The number of applied ALD cycles and the annealing temperature may play a role for the performance of the catalyst and were therefore also investigated. Upon comparing samples fabricated with 100, 300 and 500 ALD cycles, the 300-cycle sample showed the highest current intensity (Figure S9a). The lower number of ALD cycles (100) obviously resulted in too low amounts of active  $\text{Co}_x\text{O}_y$ , while the density of deposited  $\text{Co}_3\text{O}_4$  was too high after 500 applied ALD cycles (Figure S1c), resulting in larger nanoparticles after annealing, which decreases the reactivity. The annealing temperature had a similar effect on the size of the  $\text{Co}_x\text{O}_y$  nanoparticles. After annealing at 800 °C,  $\text{Co}_x\text{O}_y/\text{CNT}@C$  showed lower current densities in comparison to the samples annealed at 600 °C (Figure S10). The higher temperature enhanced the mobility of the nanoparticles and induced merging into larger particles as a result of Ostwald ripening (Figure S10 d).

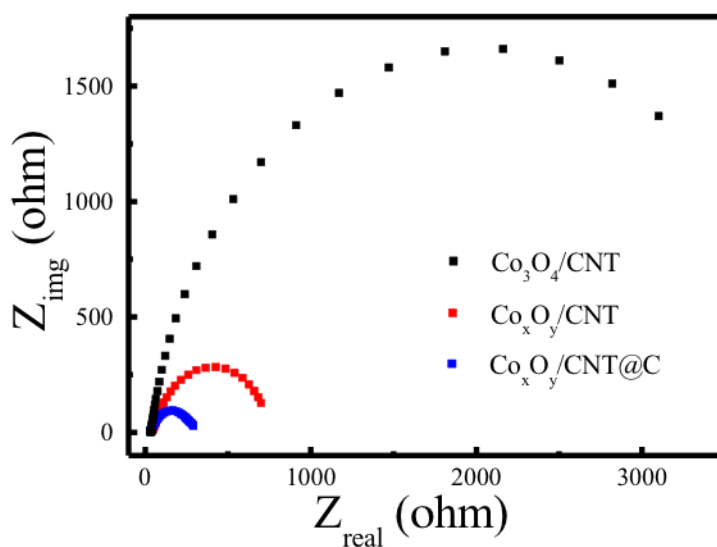


Figure S11 Electrochemical impedance spectroscopy (EIS) of ORR recorded with the  $\text{Co}_3\text{O}_4/\text{CNT}$ , the  $\text{Co}_x\text{O}_y/\text{CNT}$ s and  $\text{Co}_x\text{O}_y/\text{CNTs@C}$  in oxygen-saturated 0.1 M KOH solution at 1600 rpm at a potential of -0.15 V vs. Ag/AgCl.

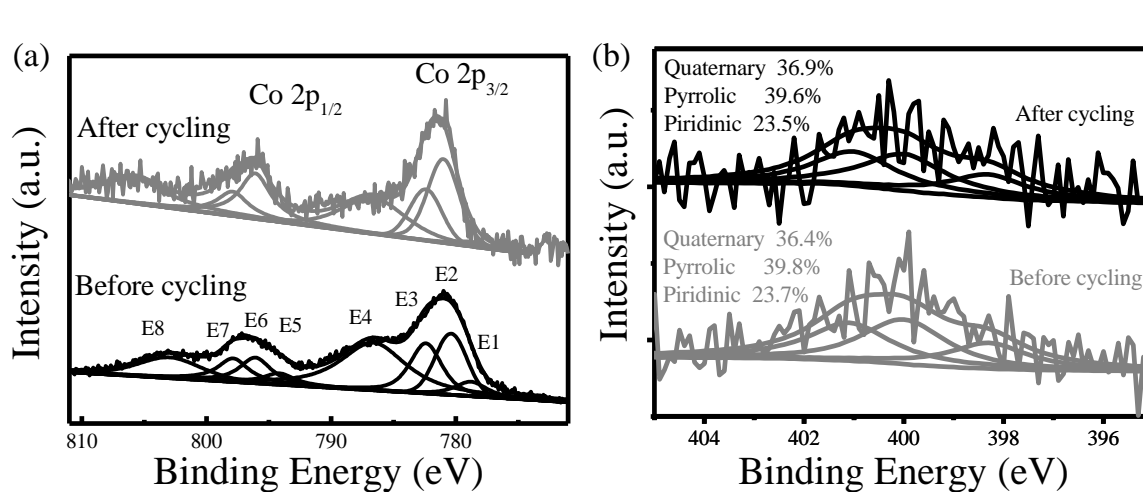


Figure S12. XPS spectra of  $\text{Co}_x\text{O}_y/\text{CNT@C}$  before and after 10000 cycles of cycling test, (a) Co 2p E1-E8 corresponds to  $2p_{3/2}$  of Co metal, Co(II), Co (III), satellite of Co  $2p_{3/2}$ ,  $2p_{1/2}$  of Co metal, Co(II), Co(III) and satellite of Co  $2p_{1/2}$ , respectively, (b) N 1s.

Table S1 Comparison of electrocatalytic activity and stability/durability of embedded cobalt oxide based catalysts recently reported for ORR in alkaline media.

Catalyst	Loading density (mg/cm <sup>2</sup> )	Reactivity			Stability			Reference
		Half-wave potential vs. RHE from 1600 rpm LSV	Cathodic current density at 0.5 V vs. RHE from 1600 rpm LSV	Tafel slope in low over potential region	ECSA retention over cycling test	Half-wave potential shift over cycling test	Chrono-amperometric test at 1600 RPM	
Co <sub>x</sub> O <sub>y</sub> /CNT@NC	0.2	0.80 V 70 mV negative than Pt/C	~ 5.4 mA/cm <sup>2</sup>	58 mV/decade	86% after 10,000 cycles	10 mV after 5000 cycles, 21 mV after 10000 cycles	0.65 V vs RHE 17% loss after 100000 s	<b>This work</b>
Co@Co <sub>3</sub> O <sub>4</sub> /NC	0.21	0.83 V 70 mV negative than Pt/C	< 5 mA/cm <sup>2</sup>	NA	NA	NA	NA	<i>Angew. Chem. Int. Ed.</i> 2016, <b>55</b> , 4087-4091
CoP-CMP	0.6	10 mV negative than Pt/C	< 5 mA/cm <sup>2</sup>	NA	96.7% after 1000 cycles	NA	NA	<i>Adv. Mater.</i> 2014, <b>26</b> , 1450-1455
Co@Co-N-C	0.6	0.879 V 2 mV negative than Pt/C	< 5 mA/cm <sup>2</sup>	59 mV/decade	NA	17 mV after 2000 cycles	-0.3V vs. RHE 10% loss after 20000 s	<i>Chem. Commun.</i> 2015, <b>51</b> , 8942-8945
Co@Co <sub>3</sub> O <sub>4</sub> /BN CNTs	~ 0.7	NA	< 5 mA/cm <sup>2</sup>	83 mV/decade	NA	NA	-0.40 V vs. Hg/HgO 19.4% loss over 20000 s	<i>Nanoscale.</i> 2015, 7,7056-64.
Co/CoO/CoFe <sub>2</sub> O <sub>4</sub> /G	0.28	50 mV negative than Pt/C	< 4 mA/cm <sup>2</sup>	NA	NA	NA	-0.2 V vs. Ag/AgCl 20% loss after 20000 s test	<i>Nanoscale.</i> 2014, <b>6</b> , 203-206
Co/N/C	0.458	0.80 V 25 mV negative than Pt/C	~ 4.5 mA/cm <sup>2</sup>	NA	NA	NA	NA	<i>Sci. Rep.</i> 2014, <b>4</b> , 4386
Co <sub>10</sub> -NMCV	0.15	20 mV negative than Pt/C	~ 4 mA/cm <sup>2</sup>	59.64 mV/decade	NA	Eonset shift 24 mV for 6000 cycles	-0.35 V vs. Ag/AgCl ~ 15% after 20000s	<i>J. Mater. Chem. A</i> 2014, <b>2</b> , 11672-11682

Address correspondence to Lianbing Zhang, lzhang@nanogune.eu; Mato Knez, m.knez@nanogune.eu